Research Square

Preprints are preliminary reports that have not undergone peer review.
They should not be considered conclusive, used to inform clinical practice,
or referenced by the media as validated information.

Understanding the reaction mechanism of the CO2 and cyclohexene oxide copolymerization catalyzed by zinc(II) and magnesium(II) catalysts: a DFT approach

Lucas W. de Lima
Universidade de Sao Paulo Instituto de Quimica
Sara Figueirêdo de Alcântara Morais
Universidade de Sao Paulo Instituto de Quimica
Ataualpa A. C. Braga (ataualpa@iq.usp.br)
Universidade de São Paulo Instituto de Química: Universidade de Sao Paulo Instituto de Quimica
https://orcid.org/0000-0001-7392-3701

Research Article

Keywords: CO2, ROCOP, bimetallic catalyst, DFT

Posted Date: June 8th, 2022

DOI: https://doi.org/10.21203/rs.3.rs-1713986/v1

License: This work is licensed under a Creative Commons Attribution 4.0 International License.
Read Full License

Understanding the reaction mechanism of the CO_2 and cyclohexene oxide copolymerization catalyzed by zinc(II) and magnesium(II) catalysts: a DFT approach

Lucas W. de Lima[1], Sara Figueirêdo de Alcântara Morais[1] and Ataualpa A.C. Braga[1*†]

[1]Institute of Chemistry, University of São Paulo, Lineu Prestes Av.,748, São Paulo, 05508-900, São Paulo-SP, Brazil.

*Corresponding author(s). E-mail(s): ataualpa@iq.usp.br;
Contributing authors: lucas.welington.lima@usp.br;
saramorais@iq.usp.br;
†These authors contributed equally to this work.

Abstract

The reaction mechanisms of carbon dioxide and cyclohexene oxide copolymerization catalyzed by four different zinc(II)-magnesium(II) catalysts were computationally studied using the density functional theory at the BP86-D3(BJ)/def2-TZVP/SMD//BP86-D3(BJ)/def2-SVP/SMD level of theory. The results showed that the most effective catalyst was the ZnMg system, in which poly(cyclohexene carbonate) was the preferred product, followed by the side product *cis*-cyclohexene carbonate. The QTAIM, NCI and ELF analysis performed to understand the role of metals in the reaction showed that ligands and substrates interact more strongly with zinc(II) centers compared to magnesium(II) centers. Furthermore, the Zn-I interaction at the M_1 position was stronger than the Mg-I interaction at the same position. All these results indicate a synergism between the metals Zn and Mg, which makes Zn(II)Mg(II) the best combination for the reaction.

Keywords: CO_2, ROCOP, bimetallic catalyst, DFT

1 Introduction

The industrialization process faced since the 18th century has generated social and environmental changes that have brought significant challenges, which is leading us to a climate that is increasingly less suitable for life on Earth. Due to the generation of energy based on the burning of fossil fuels, the concentrations of carbon dioxide (CO_2) in the atmosphere have increased c.a. 75% since the 18th century, scenario that contributed significantly with the rise in the average global surface temperature by 0.6 °C in the last century [1–3]. Aiming to find solutions to overcome this alarming situation, scientists around the world are trying to reduce CO_2 emissions into the atmosphere by different strategies. Among the viable alternatives of CO_2 conversion, the chemical conversion into valuable products is already an relevant industrial process that uses CO_2 to synthesize products like salicylic acid, methanol, cyclic carbonates, urea and polymers such as polyether carbonates and polycarbonates [2, 4].

Although the conversion of CO_2 into products will never be capable of compensate its emissions in the atmosphere, the conversion into materials that have large use in society such as polymers is an interesting alternative to mitigate the problem [3]. Polymers play a central role in modern societies in areas that have a wide range of uses, from personal uses, such as clothing, to materials used in the fabrication of water cleaners. The use of carbon dioxide as a reagent for the production of polymers has already reached the status of a commercial product, being an environmental alternative to polymers synthesized from petrochemical sources [5].

Ring opening and copolymerization reactions (ROCOP) employing CO_2 and a cyclic epoxide such as cyclohexene carbonate (CHO) as a promising reaction to both use carbon dioxide as a reagent and to produce poly-(cyclohexene carbonate) via a less harmful route than the traditional route that uses phosgene gas and trans-diols such as bisphenol A in synthesis [3]. Bimetallic homogeneous catalysts are being employed to promote the ROCOP of CO_2 and CHO. The use of bimetallic catalysts rely on the synergistic effects between metals that are used to activate chemical bonds that in a single metal catalyst would not happen [6].

In Figure 1 is presented the general scheme of the ROCOP reaction and the catalyst used in this work. The main product of these reactions, as described in Figure 1, is poly(cyclohexene carbonate), and a minor product is formed in a side reaction, the *cis*-cyclohexene carbonate. The catalyst employed in this reaction is composed by two metals described in Figure 1 as metals 1 (M_1) and 2 (M_2), in which homo- or hetero-bimetallic combinations could be used [4]. Combinations such as Zn(II)Zn(II) [7], Mg(II)Mg(II) [8, 9], Ti(IV)Zn(II) [10], Fe(III)Fe(III) [11], Co(III)Co(II), Co(II)Co(II) [12], and Co(II)Mg(II) [9] were used at metal positions 1 and 2.

This work aims to study the reaction mechanism of the ROCOP catalysed by bimetallic homogeneous catalysts composed of zinc(II) and magnesium(II) in homo- and hetero-bimetallic combinations (from now on named as MgMg,

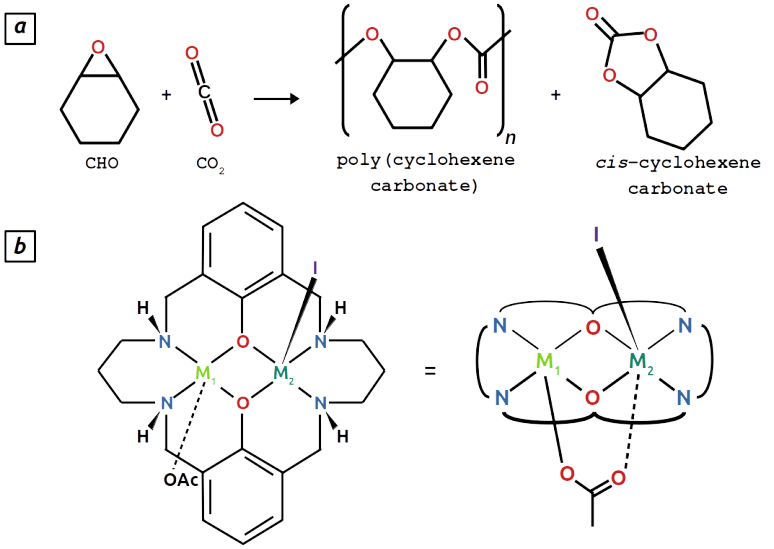

Fig. 1 a) General scheme of the ring opening and copolymerization reaction (ROCOP) of CO_2 and CHO. b) Catalyst used in the reaction and its simplified representation

ZnMg, MgZn and ZnZn systems) by means of computational modelling employing the density functional theory (DFT) in calculations.

2 Methods

2.1 Computational details

All geometry optimizations, vibrational frequencies, and single point calculations were performed with ORCA 4.2 software [13, 14] using the BP86 [15–17] density functional approximation (DFA) along with the def2-TZVP and def2-SVP basis set [18] for single point and geometry optimization/frequency calculations. Dispersion effects were accounted for using the D3 dispersion correction with Beck-Johnson damping [19, 20]. Solvation effects were modeled by the implicit solvation model SMD using the parameters for the dibutyl ether solvent [21]. To accelerate the calculation of Coulomb and exchange integrals, the resolution of identity (RI) approximation [22–27] was used, in which the def2/J auxiliary basis set [28] was used to perform the RI approximation. To reach this level of theory, a benchmark was made comparing the performance of ten selected DFAs, where the results of this study can be found in the supplementary material.

Since some molecules in the catalytic cycle are non-rigid, a conformational analysis using CREST software [29] was performed prior to DFT geometry optimization and subsequent frequency calculation. The intermediaries **Int3**, **Int6a**, **Int7a** and the first monomer of the polymer produced in the reaction were submitted to this analysis and the structure with the lowest energy was

taken as the initial structure for the DFT calculation. Conformational analysis and thermal corrections for the DFT calculations were performed at 393.15 K, the temperature commonly held in experiments in analogous systems. The transition states were identified as having only one imaginary eigenvalue of the hessian and confirmed by the IRC algorithm [30].

The final Gibbs free energy (G) for each molecule was calculated using the expression:

$$G = E_{elec} + G_{corr} + \Delta G^{o}_{solv} \quad (1)$$

where E_{elec} is the electronic energy of the molecule at the BP86-D3(BJ)/def2-TZVP/SMD level of theory, the G_{corr} is the thermal corrections from the frequency calculations at the BP86-D3(BJ)/def2-SVP/SMD level of theory and ΔG^{o}_{solv} is the correction to bring the molecules from the gas phase to solution at a concentration of 1 mol·L^{-1} in which the calculated value for 393.15 K is 10.5 kJ·mol^{-1}.

QTAIM and ELF calculations and plots were performed using Multiwfn 3.8 software [31]. The NCI index analysis was performed using the NCIPLOT4 software [32]. Structure images were generated using ChimeraX software [33, 34] along with SEQCROW [35, 36] and in VMD 1.9.4a55 software [37].

3 Results and discussion

3.1 Catalytic cycle

In this article, two main products have their reaction mechanisms considered according to the experimental results on analogous systems [4, 7, 8]: i) the catalytic cycle of poly(cyclohexene carbonate) formation (represented in Figure 2 as the green path); and ii) the catalytic cycle of *cis*-cyclohexene carbonate formation (represented as the orange path in Figure 2). Both catalytic cycles have common steps that are represented as the black path, which comprehends the formation of intermediaries 1 (**Int1**), 2 (**Int2**), 3 (**Int3**) and 4 (**Int4**).

The first step of the reaction is due to the coordination of a CHO molecule with the catalyst, which forms **Int1**; After the formation of **Int1**, **Int2** is formed through **TS1** by opening the CHO epoxide ring. With the coordination of CO_2 in M_1 in **Int2**, **Int3** is formed, subsequently forming **Int4** by a nucleophilic attack of the oxygen bonded to M_2 in the CO_2 carbon atom passing through **TS2**. Up to this point, the reaction could take two different paths, forming the poly(cyclohexene carbonate) or *cis*-cyclohexene carbonate. The formation of the poly(cyclohexene carbonate) occurs by first coordinating one more molecule of CHO, forming intermediary 5a (**Int5a**), and next forming intermediary 6a (**Int6a**) via a second CHO epoxide ring opening reaction passing through transition state 3a (**TS3a**), begining the polymer propagation. Thus, to produce more monomers of the polymer, more molecules of CHO coordinate to M_1, subsequently reacting to open the CHO epoxide ring. In this work we restricted ourselves to only one propagation step since other propagation steps are similar to the first one. Finally, we proposed a termination

step to the reaction in which one acetic acid molecule coordinates to M_2 forming the intermediary 7a (**Int7a**), and after a proton transfer reaction through transition state 4a (**TS4a**) forming the intermediary 8a (**Int8a**), eventually regenerating the catalyst and liberating the first monomer of poly(cyclohexene carbonate).

The formation of *cis*-cyclohexene carbonate proceeds by, firstly, a geometrical rearrangement of **Int4a**, forming thus the intermediary 5b (**Int5b**). After, by a backbiting reaction, the intermediary 6b (**Int6b**) is formed passing through the transition state 3b (**TS3b**). Finally, the catalyst is regenerated and the *cis*-cyclohexene carbonate molecule is released.

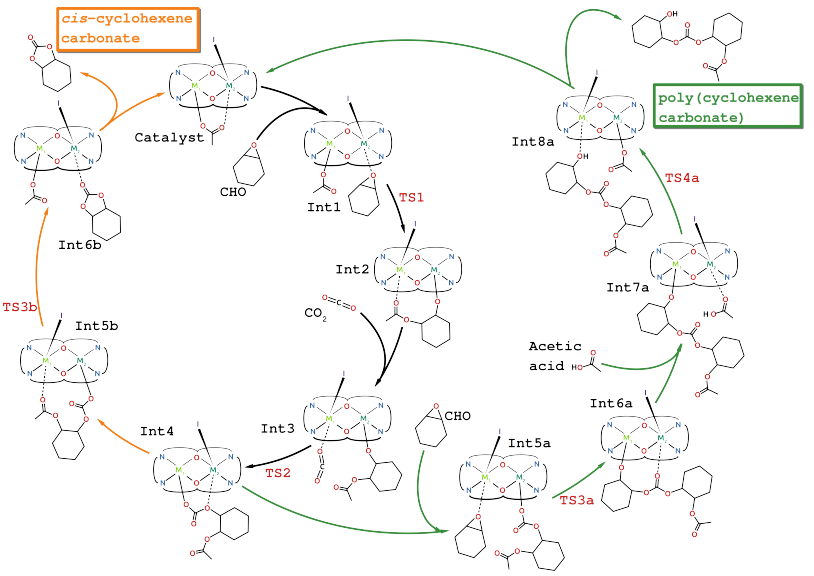

Fig. 2 Catalytic cycle for the reactions considered in this work. The black path is common between the two cycles, in which the green path is the one representing the steps of the poly(cyclohexene carbonate) formation and the orange path represents the steps of formation of *cis*-cyclohexene carbonate

3.2 Comparison between MgMg, ZnMg, MgZn and ZnZn energetic profiles

The energetic profile for the MgMg, ZnMg, MgZn and ZnZn systems is represented in Figure 3. As can be seen, the opening of the epoxide ring of the CHO molecule is a step in which all systems have similar energies and, on the other hand, the nucleophilic attack on the CO_2 carbon atom occurs with different energetic barriers in which the trends of the barriers are inversed in the second step of the reaction. A remarkable feature of the four catalytic systems is that all considered barriers are feasible to take place in the given temperature [38],

which implies that the modeled catalytic systems determine only how fast the reaction could occur.

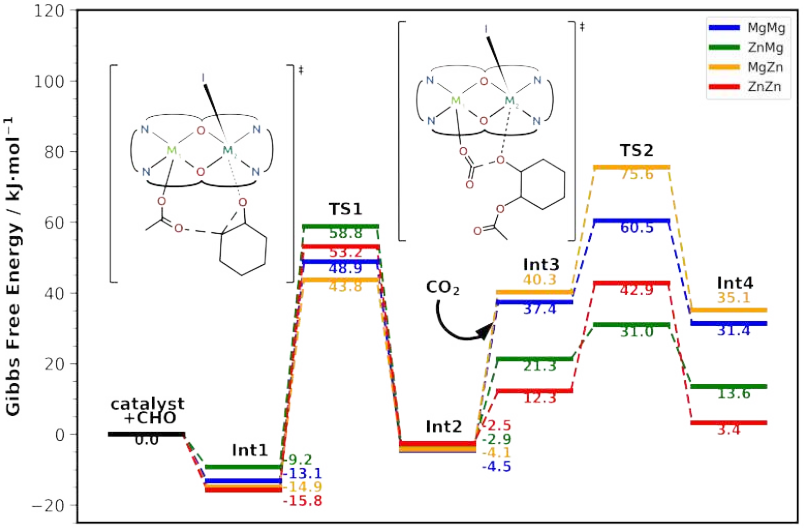

Fig. 3 Energetic profile for the MgMg, ZnMg, MgZn and ZnZn systems. Calculation at the BP86-D3(BJ)/def2-TZVP/SMD//BP86-D3(BJ)/def2-SVP/SMD level of theory

The transition states **1** and **2** for the MgMg, ZnMg, MgZn and ZnZn systems are shown in Figure 4. When analyzing the transition state structures, one can see that, especially for **TS1**, the structures are very similar, which is also reflected in the energetics of those molecules, as shown in Figure 3. On the other hand, the structures for **TS2** differ in two groups, in which the transition states of the molecules where the oxygen atom attacking CO_2 is bonded to Mg are earlier transition states than those bonded to Zn.

Taking the energetics from the intermerdiary 1 (local minimum) to the energetics of the transition states, the two main barriers of this part of the catalytic cycle can be determined: i) the barrier to reach **TS1** from **Int1** (ΔG_1); and ii) the barrier from **Int1** to **TS2** (ΔG_2). Taking the ratio ${}^{\Delta G_2}/_{\Delta G_1}$ is important to show how fast the reaction would proceed in the nucleophilic attack step on CO_2 compared to the opening of the epoxide ring of the CHO molecule because the barriers for the first part of the reaction are close to each other, and thus the second step of the reaction determines the best catalytic system. In Table 1 the calculated values of ΔG_1, ΔG_2, and ${}^{\Delta G_2}/_{\Delta G_1}$ are shown.

The values shown in Table 1 show that although the ZnMg system has the second highest value ΔG_1, ΔG_2 compensates by providing a faster reaction than the other systems, as can be seen from the value of ${}^{\Delta G_2}/_{\Delta G_1}$. The general trend for the systems is $\Delta G_1 < \Delta G_2$ for systems with Mg at M_1 position and $\Delta G_2 < \Delta G_1$ for systems with Zn at M_1.

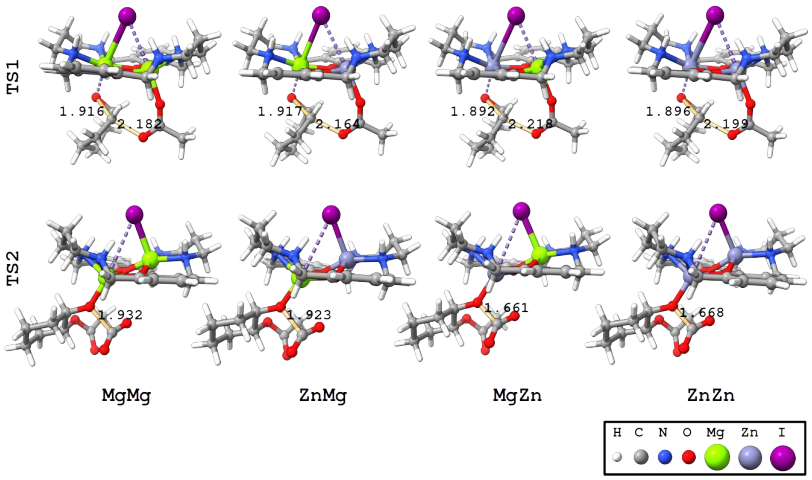

Fig. 4 Transition states **1** and **2** for the MgMg, ZnMg, MgZn and ZnZn systems. Golden bonds are those formed or broken in the reaction step, in which the bond lengths are given in angstroms

Table 1 ΔG_1, ΔG_2 and $^{\Delta G_2}/_{\Delta G_1}$ for the modeled catalytic systems

Catalytic system	ΔG_1 / kJ·mol^{-1}	ΔG_2 / kJ·mol^{-1}	$^{\Delta G_2}/_{\Delta G_1}$
MgMg	62.0	73.6	1.19
ZnMg	68.0	40.2	0.59
MgZn	58.7	90.5	1.54
ZnZn	69.0	58.7	0.85

3.3 Topological Analysis

Once the **TS2** presented such large difference between activation energies for distinct combinations of M_1-M_2, it was performed an AIM analysis of **TS2** and its previous intermediate (**Int3**) in order o evaluate the effect of metal changes (M_1 and M_2) in the strength of some highlighted chemical bonds (or interactions) beyond its influence on the reactivity of such systems. The quantum theory of atoms in molecules (QTAIM) was developed by Richard Bader [39, 40] and has been widely applied in the evaluation and characterization of chemical bonds and noncovalent interactions [41, 42]. This theory is based on the topological evaluation of the electronic density $\rho(r)$ to characterize the atoms in the properties of the molecules and their interactions. In broad terms, a chemical bond (or an interaction between atoms) can be investigated through the evaluation of its AIM properties at its Bond Critical Points (BCPs). The BCP is a critical point formed by the encounter of vector path lines of the electronic density gradient $\nabla^2\rho_{CP}$ that come from two distinct attractors (commonly atoms in a molecule). These path lines that

connect two attractors through the same BCP are called Bond Path (BP). The presence of a BP connecting two attractors between a BCP features the presence of a chemical bond or a noncovalent interaction between them. The strength of such interactions can be estimated through the AIM properties at its respective BCP.

The AIM molecular graphs of **Int3** and **TS2** (MgMg, ZnMg, MgZn, and ZnZn, respectively) revealed several covalent and noncovalent interactions between catalysts and substrates (Figures 5 and 6). Some interactions in these systems were highlighted to evaluate their AIM properties in detail, and the main interactions are displayed in Tables 2 and 3. The AIM properties for all the BCPs studied are shown in Tables S5-S12.

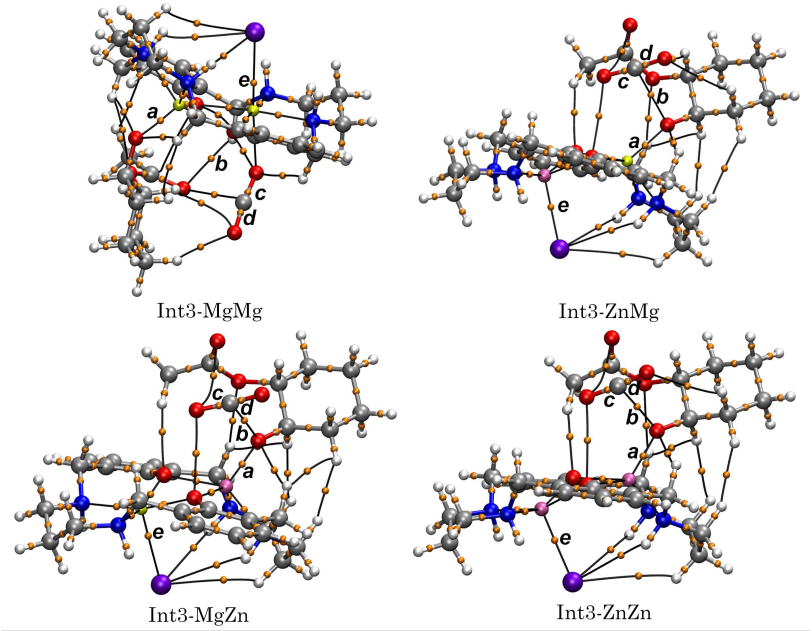

Fig. 5 AIM molecular graphs for **Int3** in the MgMg, ZnMg, MgZn and ZnZn systems. Other visualization angles can be found in the supplementary material

In general, the AIM analysis of **Int3** and **TS2** in the MgMg, ZnMg, MgZn, and ZnZn systems shows that Zn atoms have stronger interactions with O and N atoms (from the ligand). The electronic density $\rho(r)$ values of Zn-O and Zn-N bonds for **Int3** and **TS2** ranging between 0.05 and 0.07 $(e/Bohr^3)$ (BCPs $\boldsymbol{f}$, $\boldsymbol{g}$, $\boldsymbol{h}$, and $\boldsymbol{i}$ for ZnMg, BCPs $\boldsymbol{j}$, $\boldsymbol{k}$, $\boldsymbol{l}$, and $\boldsymbol{m}$ for MgZn and BCPs $\boldsymbol{f}$, $\boldsymbol{g}$, $\boldsymbol{h}$, $\boldsymbol{i}$, $\boldsymbol{j}$, $\boldsymbol{k}$, $\boldsymbol{l}$, and $\boldsymbol{m}$ for ZnZn) that are higher than equivalent $\rho(r)$ values for Mg-O and Mg-N bonds which ranged between 0.03 and 0.05 $(e/Bohr^3)$ (BCPs $\boldsymbol{f}$, $\boldsymbol{g}$, $\boldsymbol{h}$, $\boldsymbol{i}$, $\boldsymbol{j}$, $\boldsymbol{k}$, $\boldsymbol{l}$, and $\boldsymbol{m}$ for MgMg, BCPs $\boldsymbol{j}$, $\boldsymbol{k}$, $\boldsymbol{l}$, and $\boldsymbol{m}$ for ZnMg, and BCPs $\boldsymbol{f}$, $\boldsymbol{g}$, $\boldsymbol{h}$, and $\boldsymbol{i}$ for MgZn) as can be verified at Tables S5-S12. In addition to that, the Zn-O and Zn-N bonds showed $\|V_{CP}\|/G_{CP} > 1$, which indicates that

Table 2 QTAIM data for **Int3** of the MgMg, ZnMg, MgZn and ZnZn systems

Structure	Bond	BCP	ρ_{CP}	$(\nabla^2\rho_{CP})$	V_{CP}	$\left(\|V_{CP}\|/G_{CP}\right)$
MgMg	M_2-O	***a***	0.0559	0.4269	-0.0869	0.8979
ZnMg	M_2-O	***a***	0.0579	0.4471	-0.0915	0.9003
MgZn	M_2-O	***a***	0.0973	0.4954	-0.1692	1.1547
ZnZn	M_2-O	***a***	0.0965	0.4909	-0.1672	1.1534
MgMg	M_2-CO_2	***b***	0.0163	0.0632	-0.0109	0.8177
ZnMg	M_2-CO_2	***b***	0.0141	0.0467	-0.0082	0.8275
MgZn	M_2-CO_2	***b***	0.0192	0.0653	-0.0124	0.8651
ZnZn	M_2-CO_2	***b***	0.0197	0.0664	-0.0128	0.8703
MgMg	C-O	***c***	0.4428	0.0151	-1.6248	1.9954
ZnMg	C-O	***c***	0.4484	0.0613	-1.6647	1.9818
MgZn	C-O	***c***	0.4484	0.0682	-1.6667	1.9797
ZnZI	C-O	***c***	0.4489	0.0725	-1.6702	1.9785
MgMg	C-O	***d***	0.4576	0.1892	-1.7395	1.9471
ZnMg	C-O	***d***	0.4493	0.0797	-1.6727	1.9764
MgZn	C-O	***d***	0.4477	0.0556	-1.6595	1.9834
ZnZn	C-O	***d***	0.447	0.0458	-1.6539	1.9862
MgMg	I-M_1	***e***	0.0191	0.0566	-0.0147	1.0202
ZnMg	I-M_1	***e***	0.0497	0.0901	-0.0422	1.3035
MgZn	I-M_1	***e***	0.0226	0.0706	-0.0183	1.0176
ZnZn	I-M_1	***e***	0.0461	0.082	-0.0378	1.2962

Table 3 QTAIM data for **TS2** of the MgMg, ZnMg, MgZn and ZnZn systems

Structure	Bond	BCP	ρ_{CP}	$(\nabla^2\rho_{CP})$	V_{CP}	$\left(\|V_{CP}\|/G_{CP}\right)$
MgMg	M_2-O	***a***	0.0501	0.3688	-0.0733	0.8859
ZnMg	M_2-O	***a***	0.0493	0.3607	-0.0715	0.8844
MgZn	M_2-O	***a***	0.0745	0.3712	-0.1158	1.1104
ZnZn	M_2-O	***a***	0.0744	0.3698	-0.1155	1.1107
MgMg	M_2-CO_2	***b***	0.0824	0.1099	-0.0718	1.4464
ZnMg	M_2-CO_2	***b***	0.0841	0.1087	-0.0737	1.4611
MgZn	M_2-CO_2	***b***	0.1513	-0.0156	-0.1704	2.047
ZnZn	M_2-CO_2	***b***	0.1489	-0.008	-0.166	2.0243
MgMg	C-O	***c***	0.4266	-0.2272	-1.499	2.0788
ZnMg	C-O	***c***	0.4268	-0.2283	-1.4999	2.0791
MgZn	C-O	***c***	0.4108	-0.4663	-1.3679	2.1863
ZnZn	C-O	***c***	0.4121	-0.4542	-1.3771	2.1797
MgMg	C-O	***d***	0.4304	-0.1605	-1.5319	2.0538
ZnMg	C-O	***d***	0.4295	-0.1715	-1.5251	2.0579
MgZn	C-O	***d***	0.4178	-0.3672	-1.4249	2.1377
ZnZn	C-O	***d***	0.4177	-0.3652	-1.4247	2.1369
MgMg	I-M_1	***e***	0.023	0.0721	-0.0188	1.0204
ZnMg	I-M_1	***e***	0.0468	0.0828	-0.0384	1.3
MgZn	I-M_1	***e***	0.0227	0.071	-0.0184	1.0174
ZnZn	I-M_1	***e***	0.0466	0.0832	-0.0383	1.2963

Springer Nature 2021 LaTeX template

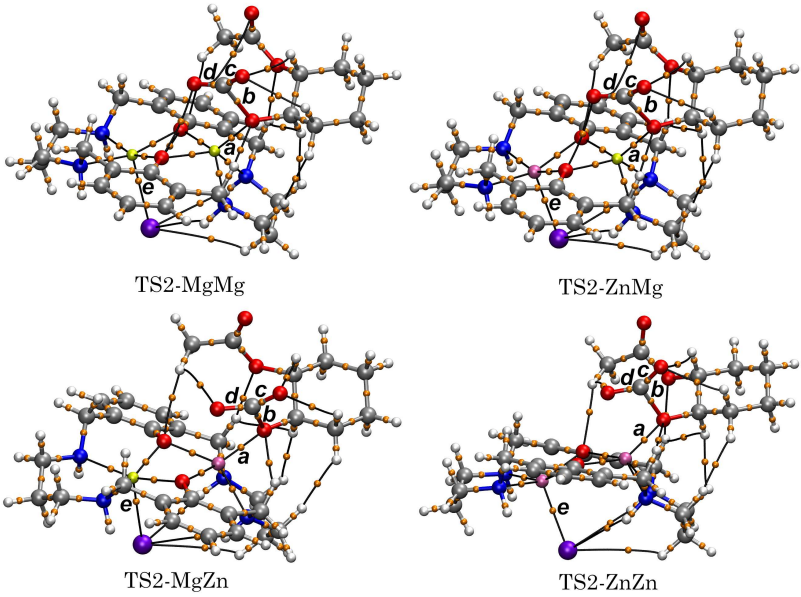

Fig. 6 AIM molecular graphs for **TS2** in the MgMg, ZnMg, MgZn and ZnZn systems. Other visualization angles can be found in the supplementary material

these interactions are covalent [43], while the Mg-O and Mg-N bonds showed $\|V_{CP}\|/G_{CP} < 1$, which indicates that these interactions are noncovalent. This behavior demonstrates that Zn atoms interact with the ligand more strongly than Mg atoms, and the strength of such interactions is reflected in the stability of the complexes and their reactivity.

The O-M_2 interaction between M_2 and O atoms of the CHO molecule (BCP ***a***) was verified to be stronger when M_2=Zn (ρ_{CP} about 0.097 ($e/Bohr^3$) for **Int3** and ρ_{CP} about 0.075 ($e/Bohr^3$) for **TS2**) than when M_2=Mg (ρ_{CP} about 0.057 ($e/Bohr^3$) for **Int3** and ρ_{CP} about 0.05 ($e/Bohr^3$) for **TS2**). Additionally, the interaction O-M_2 with Zn showed $\|V_{CP}\|/G_{CP} > 1$ (indicating covalence), whereas the interaction with Mg showed $\|V_{CP}\|/G_{CP} < 1$ (indicating noncovalence). The O-M_2 strength difference between **Int3** and **TS2** is substantially higher for Zn as M_2 than for Mg (that barely had the strength of its O-M_2 interaction changed).

Besides that, the interaction M_2-CO_2 (BCP ***b***) is stronger for Zn as M_2 then for Mg as M_2 either for CO_2 adsorbed on CHO (**Int3**) and for **TS2** in which the O-C chemical bond between O of CHO and C of CO_2 is being formed. The O-CO_2 interaction is particularly stronger for Zn as M_2 (ρ_{CP} is about 0.15 ($e/Bohr^3$) at BCP ***b*** for M_2=Zn) than for Mg (ρ_{CP} about 0.08 ($e/Bohr^3$) at BCP ***b*** for M_2=Mg) in the **TS2** structures. These results agree with the O-CO_2 bond distances and the ELF analysis presented in Figure 7 that shows higher concentration of electron density in Mg than in Zn centers, and consequently, smaller interaction between the atoms of the forming bond. The strength of the O-CO_2 interaction directly affects the bond strength of

C-O bonds of CO_2 (BCPs ***c*** and ***d***), particularly in the **TS2**. The ρ_{CP} at the BCPs ***c*** and ***d*** in the **TS2** is about 0.43 ($e/Bohr^3$) when M_2=Mg and ρ_{CP} is about 0.42 ($e/Bohr^3$) when M_2=Zn. Although this difference can seems low, by evaluating the difference between potential energy density (V_{CP}) at the BCPs ***c*** and ***d*** for M_2=Mg and M_2=Zn we can achieve a difference about 0.13 $Hartree/Bohr^3$ (or 80 kcal/mol) between **TS2** in the MgMg and in the MgZn systems that is substantial.

Finally, the AIM analysis indicates that the I-M_1 interaction is considerably stronger for M_1=Zn than for M_1=Mg, and this interaction contributes to the stabilization of **Int3** and **TS2** in the ZnMg and ZnZn systems. This behavior agrees with NCI finds that showed stronger interactions between I-Zn than I-Mg as can be verified in Figure 8 and helps to understand its stabilization. Meanwhile, the stability exchange between ZnMg and ZnZn in **TS2** could be related to the energetic balance between the two half-broken strong C-O bonds (BCPs ***c*** and ***d***) to make a new single O-C bond (BCP ***b***). The noncovalent interactions (presented in Figure 8) between catalyst, CHO and CO_2 showed weak in comparison to the interactions highlighted and should not had great role on the stabilization of systems. The AIM and NCI analysis demonstrated that the interaction between Zn and I stabilizes the system. Beyond that, the Mg as M_2 favours the reaction because low O-M_2 interaction strength and the slightly difference between O-CO_2 interactions strength for **Int3** and **TS2** which reflects on a lower difference between **Int3** and **TS2** and a lower activation barrier, which also can be observed by the results of the ASM analysis presented in the Supplementary information. Such synergy between M_1=Zn and M_2=Mg make the ZnMg a better candidate to catalyze this reaction, as verified through the other analyzes.

3.4 ZnMg full energetic profile

The full catalytic energetic profile of the ZnMg system is presented in Figure 9. As expected by the experimental results [8], the formation of the first monomer of poly(cyclohexene carbonate) is both a thermodynamic and a kinetic product. An important feature of the energetic profile is that the steps that involve the opening of the CHO epoxide ring have larger barriers compared to the reaction with CO_2, especially the opening of the first CHO epoxide ring, that is, $\Delta G^{\ddagger}_{TS1}$ configures the highest barrier to polymer formation. This trend of opening the first ring being the most energetic step in the reaction is in agreement with the experiments [9] and can be explained as being more energetic demanding than the $\Delta G^{\ddagger}_{TS3b}$ because the **TS3a** is more stabilized by the term $T\Delta S$ due to the higher number of degrees of freedom than **TS1**. The termination step proposed for this reaction seems to be a good suggestion because $\Delta G^{\ddagger}_{TS4a}$ is a feasible barrier and also because it configures an irreversible step, as there is no documented expressive formation of side products from the polymer monomers.

The backbiting reaction occurs first by the formation of intermediary 5b (**Int5b**) which is more favorable than intermediary 5a (**Int5a**); however,

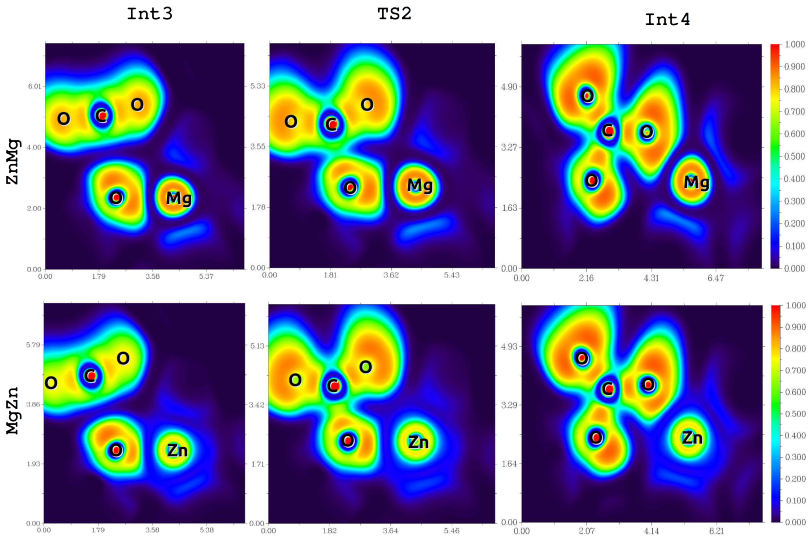

Fig. 7 ELF plots for **Int3**, **TS2**, and **Int4** in the ZnMg and MgZn systems. Length units are given in angstrom. ELF analysis was plotted only around CO_2, the O atom that attacks the CO_2 C atom and M_2, where the complete plot can be found in the supplementary material

$\Delta G^{\ddagger}_{TS3b}$ is 22.6 kJ·mol^{-1} greater than $\Delta G^{\ddagger}_{TS3a}$ and becomes the determining step of the formation of *cis*-cyclohexene carbonate. Since the barrier to **TS3b** is overcome, the formation of intermediary 6b (**Int6b**) is favorable and, like in the termination step of the polymerization reaction, the formation of **Int6b** is an irreversible step in the reaction. A notable characteristic of this path is that **Int6b** is more stable than the formation of the reaction product and the regeneration of the catalyst.

In summary, the reaction catalyzed by the ZnMg system proceeds with the formation of the first monomer of poly(cyclohexene carbonate) because this product is more stable than the *cis*-cyclohexene carbonate and also because since the reaction reaches **Int4**, passing through **TS3a** is faster than passing through **TS3b**, although **Int5b** is more stable than **Int5a**. A note about both paths is that all involved barriers are feasible to take place under experimental conditions; however, a key point, especially for path A, is that the more monomers are added to the substrate, the more the $T\Delta_r S$ term in $\Delta_r G$ contributes to stabilizing the product, and consequently, the polymer formation establishes as the most favorable product.

Taking into account the other three systems studied in this work and the reactivity presented up to the formation of **Int4**, the features of the energetic trend presented to the ZnMg systems would be similar, especially in the ZnZn system. However, in a system having both the ZnMg and the MgZn catalysts, the preferable route would be the reaction being catalyzed by ZnMg system because of the faster passage of this catalyst through **TS2**.

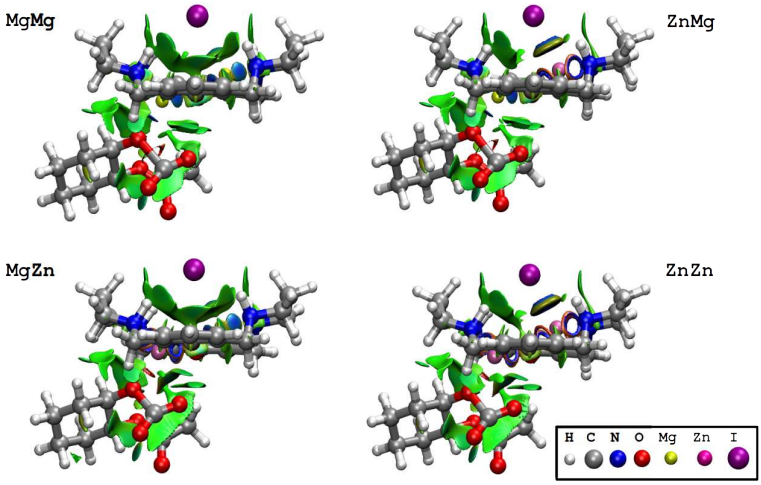

Fig. 8 Non-covalent interaction plots for **TS2** in the MgMg, ZnMg, MgZn and ZnZn systems

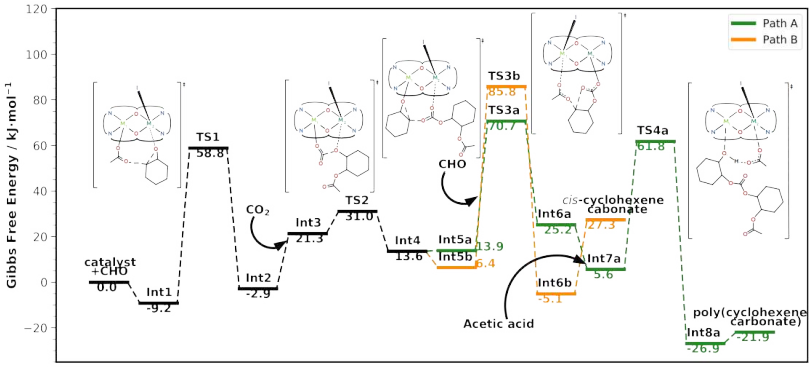

Fig. 9 Full energetic profile for the ZnMg system. In black, the common steps between both products are represented, in which the energetics for the formation of the first monomer of poly(cyclohexene carbonate) are represented in green, and the energetics for the formation of *cis*-cyclohexene carbonate are represented in orange. Calculations at the BP86-D3(BJ)/def2-TZVP/SMD//BP86-D3(BJ)/def2-SVP/SMD level of theory

4 Conclusion

The reaction mechanism of the ring opening and copolymerization of CHO and CO_2 was studied at the BP86-D3(BJ)/def2-TZVP/SMD//BP86-D3(BJ)/def2-SVP/SMD level of theory for the MgMg, ZnMg, MgZn and ZnZn systems using a model system. The characteristic that makes the ZnMg catalyst better than other studied catalysts is that the ratio $^{\Delta G_2}/_{\Delta G_1}$ is smaller for this system than for the other ones, and consequently, in reaction media that initially contained the ZnMg and MgZn system, the most probable catalyst that acts in the reaction is ZnMg. The metal in position 2 has a key role in CO_2 activation

since this metal influences directly the electron density of the oxygen atom that is attacking CO_2 carbon atom; the metal 1, on the other hand, works in the stabilization of **Int2**, and therefore the energetic demand to distort both **Int2** and CO_2 to the geometry of **TS2**.

Poly(cyclohexene carbonate) formation involves four transition states, in which the opening of the CHO epoxide ring that passes through the **TS1** is the bottleneck of the reaction, especially for ZnMg and ZnZn systems that share similar reactivities up to CO_2 activation. Already at the formation of the first monomer of poly(cyclohexene carbonate) we could observe that this is the most preferable product in the reaction and the main factor that influences in the formation of *cis*-cyclohexene carbonate is the barrier to overcome the **TS3b**.

One point that is still unclear in the studied systems is how the stereoselectivity of the polymer produced is controlled in the reactions catalyzed by the studied bimetallic catalysts. Reddi and Cramer [44] have recently studied the ROCOP of CHO and CO_2 catalyzed by an indium(III) phosphasalen catalyst and described the intricacies that promote *R,R* as the preferred product in the reaction. Therefore, we believe that promoting a better understanding of the features that promote possible poly(cyclohexene carbonate) enantiomers would be of great importance in rationalizing the stereochemistry of this polymer.

Supplementary information. The DFA benchmark, energies of each molecule calculated, and further results of activation strain and topological analyses are available in the electronic supplementary material.

Acknowledgments. The authors acknowledge the Superintendência de Tecnologia da Informação from University of São Paulo (STI-USP) and Prof. Dr. Luiz Henrique Catalani for providing computational resources that were used in part of calculations.

Author contribution. All authors contributed to the study conception and design. Material preparation, data collection and analysis were performed by Lucas W. de Lima, Sara Figueirêdo de Alcântara Morais and Ataualpa A.C. Braga. The first draft of the manuscript was written by Lucas W. de Lima and Sara Figueirêdo de Alcântara Morais, and all authors commented on previous versions of the manuscript. All authors read and approved the final manuscript.

Funding. A.A.C.B. received financial support from São Paulo Research Foundation (FAPESP) (Grants 2014/25770-6 and 2015/01491-3), the Conselho Nacional de Desenvolvimento Científico e Tecnológico (CNPq) of Brazil (Grant 312550/2020-0), and Coordenação de Aperfeiçoamento de Pessoal de Nível Superior – Brasil (CAPES) that partially supported this work (Finance Code 001). L.W.L. received financial support from CAPES for the scholarship (Grant 88887.341693/2019-00). S.F.A.M. received financial support from CNPq for the scholarship (Grant 165726/2020-2). We gratefully acknowledge support of the RCGI – Research Centre for Gas Innovation, hosted by the University of São Paulo (USP) and sponsored by FAPESP – São Paulo Research

Foundation (2014/50279-4 and 2020/15230-5) and Shell Brasil, and the strategic importance of the support given by ANP (Brazil's National Oil, Natural Gas and Biofuels Agency) through the R&D levy regulation.

Code and data availability. Inputs and outputs of the calculations presented in the article are available in ioChem-BD repository. The Python script used to perform ASM calculations is available in GitHub repository.

Declarations

The authors declare no conflicts of interest.

References

[1] Service, R.F.: The Carbon Cunundrum. Science **305**(5686), 962–963 (2004). https://doi.org/10.1126/science.305.5686.962

[2] Burkart, M.D., Hazari, N., Tway, C.L., Zeitler, E.L.: Opportunities and Challenges for Catalysis in Carbon Dioxide Utilization. ACS Catal. **9**(9), 7937–7956 (2019). https://doi.org/10.1021/acscatal.9b02113

[3] Klaus, S., Lehenmeier, M.W., Anderson, C.E., Rieger, B.: Recent advances in CO2/epoxide copolymerization—New strategies and cooperative mechanisms. Coord. Chem. Rev. **255**(13), 1460–1479 (2011). https://doi.org/10.1016/j.ccr.2010.12.002

[4] Plajer, A.J., Williams, C.K.: Heterocycle/Heteroallene Ring-Opening Copolymerization: Selective Catalysis Delivering Alternating Copolymers. Angew. Chem. Int. Ed. **61**(1), 202104495 (2022). https://doi.org/10.1002/anie.202104495

[5] Zhu, Y., Romain, C., Williams, C.K.: Sustainable polymers from renewable resources. Nature **540**(7633), 354–362 (2016). https://doi.org/10.1038/nature21001

[6] Campos, J.: Bimetallic cooperation across the periodic table. Nat. Rev. Chem. **4**, 696–702 (2020). https://doi.org/10.1038/s41570-020-00226-5

[7] Buchard, A., Jutz, F., Kember, M.R., White, A.J.P., Rzepa, H.S., Williams, C.K.: Experimental and Computational Investigation of the Mechanism of Carbon Dioxide/Cyclohexene Oxide Copolymerization Using a Dizinc Catalyst. Macromolecules **45**(17), 6781–6795 (2012). https://doi.org/10.1021/ma300803b

[8] Deacy, A.C., Durr, C.B., Garden, J.A., White, A.J.P., Williams, C.K.: Groups 1, 2 and Zn(II) Heterodinuclear Catalysts for Epoxide/CO2 Ring-Opening Copolymerization. Inorg. Chem. **57**(24), 15575–15583 (2018).

https://doi.org/10.1021/acs.inorgchem.8b02923

[9] Deacy, A.C., Kilpatrick, A.F.R., Regoutz, A., Williams, C.K.: Understanding metal synergy in heterodinuclear catalysts for the copolymerization of CO2 and epoxides. Nat. Chem. **12**(4), 372–380 (2020). https://doi.org/10.1038/s41557-020-0450-3

[10] Garden, J.C., White, A.J.P., Williams, C.K.: Heterodinuclear titanium/zinc catalysis: synthesis, characterization and activity for CO2/epoxide copolymerization and cyclic ester polymerization. Dalton Trans. **46**, 2532–2541 (2017). https://doi.org/10.1039/C6DT04193K

[11] Buchard, A., Kember, M.R., Sandeman, K.G., Williams, C.K.: A bimetallic iron(iii) catalyst for CO2/epoxide coupling. Chem. Commun. **47**, 212–214 (2011). https://doi.org/10.1039/C0CC02205E

[12] Kember, M.R., White, A.J.P., Williams, C.K.: Highly Active Di- and Trimetallic Cobalt Catalysts for the Copolymerization of CHO and CO2 at Atmospheric Pressure. Macromolecules **43**(5), 2291–2298 (2010). https://doi.org/10.1021/ma902582m

[13] Neese, F.: The ORCA program system. WIREs Comput Mol Sci **2**(1), 73–78 (2012). https://doi.org/10.1002/wcms.81

[14] Neese, F.: Software update: the ORCA program system, version 4.0. WIREs Comput Mol Sci **8**(1), 1327 (2018). https://doi.org/10.1002/wcms.1327

[15] Becke, A.D.: Density-functional exchange-energy approximation with correct asymptotic behavior. Phys. Rev. A **38**, 3098–3100 (1988). https://doi.org/10.1103/PhysRevA.38.3098

[16] Perdew, J.P.: Density-functional approximation for the correlation energy of the inhomogeneous electron gas. Phys. Rev. B **33**, 8822–8824 (1986). https://doi.org/10.1103/PhysRevB.33.8822

[17] Perdew, J.P.: Erratum: Density-functional approximation for the correlation energy of the inhomogeneous electron gas. Phys. Rev. B **34**, 7406–7406 (1986). https://doi.org/10.1103/PhysRevB.34.7406

[18] Weigend, F., Ahlrichs, R.: Balanced basis sets of split valence, triple zeta valence and quadruple zeta valence quality for H to Rn: Design and assessment of accuracy. Phys. Chem. Chem. Phys. **7**, 3297–3305 (2005). https://doi.org/10.1039/B508541A

[19] Grimme, S., Ehrlich, S., Goerigk, L.: Effect of the damping function in dispersion corrected density functional theory. J. Comput. Chem. **32**(7),

1456–1465. https://doi.org/10.1002/jcc.21759

[20] Grimme, S., Antony, J., Ehrlich, S., Krieg, H.: A consistent and accurate ab initio parametrization of density functional dispersion correction (DFT-D) for the 94 elements H-Pu. J. Chem. Phys. **132**(15), 154104 (2010). https://doi.org/10.1063/1.3382344

[21] Marenich, A.V., Cramer, C.J., Truhlar, D.G.: Universal solvation model based on solute electron density and on a continuum model of the solvent defined by the bulk dielectric constant and atomic surface tensions. J. Phys. Chem. B **113**(18), 6378–6396 (2009). https://doi.org/10.1021/jp810292n. PMID: 19366259

[22] Baerends, E.J., Ellis, D.E., Ros, P.: Self-consistent molecular Hartree—Fock—Slater calculations I. The computational procedure. Chem. Phys. **2**(1), 41–51 (1973). https://doi.org/10.1016/0301-0104(73)80059-X

[23] Dunlap, B.I., Connolly, J.W.D., Sabin, J.R.: On first-row diatomic molecules and local density models. J. Chem. Phys. **71**(12), 4993–4999 (1979). https://doi.org/10.1063/1.438313

[24] Van Alsenoy, C.: Ab initio calculations on large molecules: The multiplicative integral approximation. J. Comput. Chem. **9**(6), 620–626 (1988). https://doi.org/10.1002/jcc.540090607

[25] Kendall, R.A., Früchtl, H.A.: The impact of the resolution of the identity approximate integral method on modern ab initio algorithm development. Theor. Chem. Acc. **97**, 158–163 (1997). https://doi.org/10.1007/s002140050249

[26] Auxiliary basis sets to approximate Coulomb potentials. Chem. Phys. Lett. **240**(4), 283–290 (1995). https://doi.org/10.1016/0009-2614(95)00621-A

[27] Eichkorn, K., Weigend, F., Treutler, O., Ahlrichs, R.: Auxiliary basis sets for main row atoms and transition metals and their use to approximate Coulomb potentials. Theor. Chem. Acc. **97**, 119–124 (1997). https://doi.org/10.1007/s002140050244

[28] Weigend, F.: Accurate Coulomb-fitting basis sets for H to Rn. Phys. Chem. Chem. Phys. **8**, 1057–1065 (2006). https://doi.org/10.1039/B515623H

[29] Pracht, P., Bohle, F., Grimme, S.: Automated exploration of the low-energy chemical space with fast quantum chemical methods. Phys. Chem. Chem. Phys. **22**, 7169–7192 (2020). https://doi.org/10.1039/

C9CP06869D

[30] Ishida, K., Morokuma, K., Komornicki, A.: The intrinsic reaction coordinate. An ab initio calculation for HNC→HCN and H+CH4→CH4+H. J. Chem. Phys **66**(5), 2153–2156 (1977). https://doi.org/10.1063/1.434152

[31] Lu, T., Chen, F.: Multiwfn: A multifunctional wavefunction analyzer. J. Comput. Chem. **33**(5), 580–592 (2012). https://doi.org/10.1002/jcc.22885

[32] Boto, R.A., Peccati, F., Laplaza, R., Quan, C., Carbone, A., Piquemal, J.-P., Maday, Y., Contreras-Garcıa, J.: NCIPLOT4: Fast, Robust, and Quantitative Analysis of Noncovalent Interactions. J. Chem. Theory Comput. **16**(7), 4150–4158 (2020). https://doi.org/10.1021/acs.jctc.0c00063

[33] Pettersen, E.F., Goddard, T.D., Huang, C.C., Meng, E.C., Couch, G.S., Croll, T.I., Morris, J.H., Ferrin, T.E.: UCSF ChimeraX: Structure visualization for researchers, educators, and developers. Protein Sci. **30**(1), 70–82 (2021). https://doi.org/10.1002/pro.3943

[34] Goddard, T.D., Huang, C.C., Meng, E.F. Elaine C. Pettersen, Couch, G.S., Morris, J.H., Ferrin, T.E.: UCSF ChimeraX: Meeting modern challenges in visualization and analysis. Protein Sci. **27**(1), 14–25 (2018). https://doi.org/10.1002/pro.3235

[35] Schaefer, A.J., Ingman, V.M., Wheeler, S.E.: SEQCROW: A ChimeraX bundle to facilitate quantum chemical applications to complex molecular systems. J. Comput. Chem. **42**(24), 1750–1754 (2021). https://doi.org/10.1002/jcc.26700

[36] Ingman, V.M., Schaefer, A.J., Andreola, L.R., Wheeler, S.E.: QChASM: Quantum chemistry automation and structure manipulation. WIREs Comput Mol Sci **11**(4), 1510 (2021). https://doi.org/10.1002/wcms.1510

[37] VMD: Visual molecular dynamics. J. Mol. Graph. **14**(1), 33–38 (1996). https://doi.org/10.1016/0263-7855(96)00018-5

[38] Ryu, H., Park, J., Kim, H.K., Park, J.Y., Kim, S.-T., Baik, M.-H.: Pitfalls in Computational Modeling of Chemical Reactions and How To Avoid Them. Organometallics **37**(19), 3228–3239 (2018). https://doi.org/10.1021/acs.organomet.8b00456

[39] Bader, R.F.W., Bader, R.F.: Atoms in Molecules: A Quantum Theory. International series of monographs on chemistry

[40] Bader, R.F.W.: A quantum theory of molecular structure and its applications. Chem. Rev. **91**(5), 893–928 (1991). https://doi.org/10.1021/cr00005a013

[41] Kumar, V..S.V. P. Shyam Vinod; Raghavendra: Bader's Theory of Atoms in Molecules (AIM) and its Applications to Chemical Bonding. J. Chem. Sci. **128**(10), 1527–1536 (2016). https://doi.org/10.1007/s12039-016-1172-3

[42] Mounssef Jr., B., de Alcântara Morais, S.F., de Lima Batista, A.P., de Lima, L.W., Braga, A.A.C.: DFT study of H2 adsorption at a Cu-SSZ-13 zeolite: a cluster approach. Phys. Chem. Chem. Phys. **23**, 9980–9990 (2021). https://doi.org/10.1039/D1CP00422K

[43] Espinosa, E., Alkorta, I., Elguero, J., Molins, E.: From weak to strong interactions: A comprehensive analysis of the topological and energetic properties of the electron density distribution involving X–HF–Y systems. J. Chem. Phys. **117**(12), 5529–5542 (2002). https://doi.org/10.1063/1.1501133

[44] Reddi, Y., Cramer, C.J.: Mechanism and Design Principles for Controlling Stereoselectivity in the Copolymerization of CO2/Cyclohexene Oxide by Indium(III) Phosphasalen Catalysts. ACS Catal. **11**(24), 15244–15251 (2021). https://doi.org/10.1021/acscatal.1c04619

Supplementary Files

This is a list of supplementary files associated with this preprint. Click to download.

- SIJMM31MAY22.pdf